Inorganic Chemistry

Article

pubs.acs.org/IC

Synthesis, Crystal Structure, and Electronic Properties of High-Pressure PdF_2-Type Oxides MO_2 (M = Ru, Rh, Os, Ir, Pt)

Yuichi Shirako,*[,†,○] Xia Wang,[‡,◆] Yoshihiro Tsujimoto,[§] Kie Tanaka,[†] Yanfeng Guo,[‡,¶] Yoshitaka Matsushita,[∥,△] Yoshihiro Nemoto,[⊥] Yoshio Katsuya,[∥] Youguo Shi,[‡,#] Daisuke Mori,[†] Hiroshi Kojitani,[†] Kazunari Yamaura,[‡,▽] Yoshiyuki Inaguma,[†] and Masaki Akaogi[†]

[†]Department of Chemistry, Gakushuin University, 1-5-1 Mejiro, Toshima-ku, Tokyo 171-8588, Japan

[‡]Superconducting Properties Unit and [§]Materials Processing Unit, National Institute for Materials Science, 1-1 Namiki, Tsukuba, Ibaraki 305-0044, Japan

[∥]NIMS Beamline Station at SPring-8, National Institute for Materials Science, 1-1-1 Kouto, Sayo-cho, Hyogo 679-5148, Japan

[⊥]Research Network and Facility Services Division, National Institute for Materials Science, 1-2-1 Sengen, Tsukuba, Ibaraki 305-0047, Japan

[#]Institute of Physics, Chinese Academy of Sciences, Beijing 100190, People's Republic of China

[▽]Graduate School of Chemical Science and Engineering, Hokkaido University, Sapporo, Hokkaido 060-0810, Japan

Supporting Information

ABSTRACT: The polycrystalline MO_2's (HP-PdF_2-type MO_2, M = Rh, Os, Pt) with high-pressure PdF_2 compounds were successfully synthesized under high-pressure conditions for the first time, to the best of our knowledge. The crystal structures and electromagnetic properties were studied. Previously unreported electronic properties of the polycrystalline HP-PdF_2-type RuO_2 and IrO_2 were also studied. The refined structures clearly indicated that all compounds crystallized into the HP-PdF_2-type structure, $M^{4+}O^{2-}{}_2$, rather than the pyrite-type structure, $M^{n+}(O_2)^{n-}$ ($n < 4$). The MO_2 compounds (M = Ru, Rh, Os, Ir) exhibited metallic conduction, while PtO_2 was highly insulating, probably because of the fully occupied t_{2g} band. Neither superconductivity nor a magnetic transition was detected down to a temperature of 2 K, unlike the case of 3d transition metal chalcogenide pyrites.

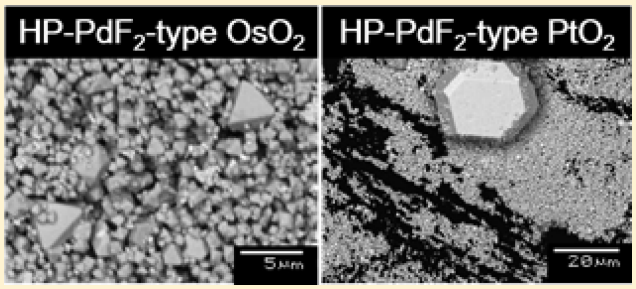

1. INTRODUCTION

A crystal structure generally specifies not only the packing conditions (space group and approximate atomic positions) but also the bonding nature and, occasionally, the valence. For example, the space group, number of sites, and atoms in the unit cell of $CaCl_2$- and ReO_3-type structures are the same as those of marcasite (FeS_2 *Pnnm*) and unfilled skutterudite ($CoAs_3$) structures, respectively. However, the last two structures have cluster anions such as the $(S_2)^{2-}$ dimer and $(As_4)^{4-}$ tetramer while $CaCl_2$- and ReO_3-type structures are constructed from only monatomic ions. Similarly, although pyrite (FeS_2 $Pa\bar{3}$) and high-pressure PdF_2 (HP-PdF_2) structures,[1,2] as drawn by VESTA[3] in parts a and b of Figure 1, respectively, share the same space group ($Pa\bar{3}$), these are differentiated by the absence/presence of anion dimers. As discussed in ref 4, the two structures can be readily distinguished by the atomic fractional coordinates of the anion (although both structures are called "pyrite"). The PdF_2 form at ambient pressure is incidentally a rutile-type structure.[1,2] The interanionic interaction (X−X attraction or repulsion) constrains the tilt angle of MX_6 octahedral linkages and bond angles of inter- and intra-MX_6 octahedra and determines the formation of either the distorted tetrahedral X_2M_3 in a pyrite-type structure or almost triangular planar XM_3 in the HP-PdF_2-type structure.

Figure 1 represents the crystal structures of MX_2 compounds. One of the features of HP-PdF_2- and pyrite-type structures is that these are composed of corner-shared MX_6 octahedra, while the other major MX_2 structures (i.e., rutile-type and related ones such as the löllingite-, $CoSb_2$-, and α-PbO_2-type structures (Figure 1c), and layered structures such as the CdI_2-type structure (Figure 1d)) include edge-shared MX_6 octahedra. In addition, HP-PdF_2- and pyrite-type structures have cubic symmetry, in contrast to rutile-like pseudo-1D tunnel and pseudo-2D layered structures such as the CdI_2-type structure.

HP-PdF_2 compounds have been mainly studied in planetary science, high-pressure crystal chemistry, and crystallography. The rutile-type SiO_2 (stishovite) transforms into the HP-PdF_2-type SiO_2 at a pressure of ~260 GPa, via $CaCl_2$- and α-PbO_2-type (seifertite)[5] structures. The HP-PdF_2-type SiO_2 is thought to be the major component of the deep mantle of a super-Earth;[6] thus,

Received: July 24, 2014
Published: October 22, 2014

   dx.doi.org/10.1021/ic501770g | *Inorg. Chem.* 2014, 53, 11616−11625

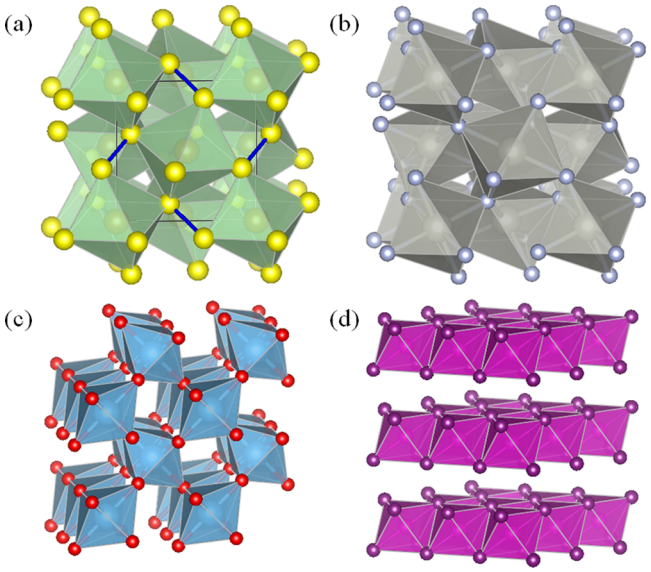

Figure 1. Crystal structures of MX_2 with MX_6 octahedra drawn by the software VESTA:[3] (a) pyrite type (deep blue thick solid lines indicate X−X bonds); (b) HP-PdF_2 type; (c) rutile type; (d) CdI_2 type.

investigations into the nature of this material would provide a better understanding of the deeper mantle. However, the HP-PdF_2-type SiO_2 exists only in extreme conditions that cannot be easily reproduced in the laboratory. It is therefore necessary to find a material that exhibits analogous transitions under more practical conditions. In fact, SiO_2 with the $Pa\bar{3}$ space group was incorrectly termed pyrite-type SiO_2 in previous work, since it does not have O−O covalent bonds.[5]

In addition, materials scientists have recently paid attention to a compound with the HP-PdF_2 structure. In a sequence of ordinary high-pressure-induced phase transitions of MX_2, the HP-PdF_2 structure is the densest structure among the compounds that consist of six-coordinated M atoms.[7] Indeed, most of the pressures are greater than 300 GPa, as indicated by the bulk moduli of a few HP-PdF_2-type compounds that have already been reported.[8] Therefore, HP-PdF_2-type compounds have recently attracted renewed attention for use as ultrahard materials with a high bulk modulus.

The electronic properties of HP-PdF_2-type compounds have rarely been reported, in contrast to the numerous crystallographic investigations. The magnetic susceptibility of HP-PdF_2-type compounds was only reported for PdF_2, which was found to be antiferromagnetic ($T_N \approx 190$ K).[2] On the other hand, pyrite-type compounds have attracted much attention in condensed matter science since the 1970s, owing to their strongly correlated electronic features. The late 3d transition metal dichalcogenides ($M^{2+}Ch_2^{2-}$: M = Mn, Fe, Co, Ni, Cu, Zn; Ch = S, Se, Te), which crystallize into a pyrite-type structure, have been systematically investigated to assess their electron counts n_e (e_g electron) and U/W, where U is the Coulomb repulsion energy and W is the bandwidth.[9−12] It has been suggested that the U/W values of the dichalcogenides are in the vicinity of the metal−insulator boundary. Thus, quantum critical phenomena, such as metal−insulator transition (MIT) and superconductivity, are expected to be features of the dichalcogenides and other closely related compounds. Superconductivity has been discovered in $CuCh_2$ (Ch = S, Se, Te)[11−15] and $M_{1-x}Ch_2$ (M = Rh, Ir; Ch = Se, Te),[16−18] and MIT has been observed in $NiS_{1-x}Se_x$.[19] Therefore, these compounds have great potential for advanced applications in the fields of condensed matter science and materials technology.

Twelve pyrite-type $M^{2+}O_2^{2-}$ and $M^{+}O_2^{-}$ (NaO_2, MgO_2, ZnO_2, CdO_2, and PaO_2) and HP-PdF_2-type $M^{4+}(O^{2-})_2$ (SiO_2, GeO_2, RuO_2, SnO_2, IrO_2, PbO_2, and UO_2) oxides have been synthesized to date, seven of which (NaO_2, MgO_2, ZnO_2, RuO_2, CdO_2, PaO_2, and UO_2) have been successfully quenched under ambient conditions.[5,8,20−27] Furthermore, three of the compounds (RuO_2, PaO_2, and UO_2) have unpaired electrons in their structure.

In general, 4d and 5d atoms exhibit significant, radially extended valence orbitals and large spin−orbit couplings in comparison with 3d atoms, leading to an increase in W. In contrast, the 2p orbital of oxygen is smaller than the 3p, 4p, and 5p orbitals of S, Se, and Te, respectively, resulting in a decrease in W. As a balance of opposing factors, the U/W values for the pyrite- and HP-PdF_2-type 4d and 5d oxides may be comparable with those of the late 3d transition metal dichalcogenides, which show noticeable electromagnetic properties.[9−15,19]

Therefore, quenchable HP-PdF_2-type MO_2 not only may be available for such geophysical and planetary studies because it crystallizes into the isostructure of the densest form of silica with SiO_6 octahedra[5] but may also exhibit interesting physical properties such as those of pyrite compounds. In spite of having a structure in the major stream of the pressure-induced structural transition map of MX_2 compounds,[7] only a few HP-PdF_2 compounds that are quenchable to ambient pressure have been reported.

In this paper, we report the synthesis, crystal structures, and electromagnetic properties of HP-PdF_2-type MO_2 (M = Ru, Rh, Os, Ir, Pt). To the best of our knowledge, the HP-PdF_2-type OsO_2, RhO_2, and PtO_2 have been synthesized for the first time. In addition, the HP-PdF_2-type IrO_2 was recovered under ambient conditions for the first time. Since details on the electronic properties of the HP-PdF_2-type RuO_2 were not revealed, although its synthesis was touched upon in a previous work,[23] the compound was included in the investigation of the electronic properties of HP-PdF_2-type MO_2. The compounds with unpaired electrons (M = Ru, Rh, Os, Ir) showed metallic conductivity, suggesting U/W values comparable with those of the late 3d transition metal dichalcogenides. It is suggested that 4d and 5d oxides crystallizing in the HP-PdF_2-type structure are applicable in the fields of condensed matter science, materials technology, and planetary science.

2. MATERIALS AND EXPERIMENTAL METHODS

2.1. Sample Preparation. Polycrystalline MO_2 (M = Ru, Os, Ir) and powdered PtO_2 with the HP-PdF_2-type structure were directly synthesized from commercial powders of rutile-type RuO_2 (76.8 wt % Ru, Wako Pure Chemical Industries), rutile-type IrO_2 (85.5 wt % Ir, Soekawa Chemicals), rutile-type OsO_2 (83 wt % Os, Alfa Aesar), and amorphous PtO_2 (85.9 wt % Pt, Furuya Metal), with $KClO_4$ (99.5%, Wako Pure Chemical Industries) as a reduction inhibitor, using a Kawai-type, multianvil, high-pressure apparatus at Gakushuin University. Each precursor was sealed in a Pt capsule, which was placed in the central part of a high-pressure cell assembled with an MgO octahedral pressure medium, $LaCrO_3$ thermal insulator tube, Pt cylindrical heater, $LaCrO_3$ plugs, BN inner sleeve, and thermocouple (Pt−Pt/13% Rh). Tungsten carbide anvils with a truncated edge length of 5 mm were used. The sample cell was kept at 17 GPa and 1273 K for RuO_2, OsO_2, and IrO_2 and 1173 K for PtO_2 for 30 min, followed by quenching to room temperature and decompression. The recovered PtO_2 was washed with pure water to remove the byproduct KCl.

Pelletized polycrystalline MO_2 species (M = Rh, Pt) were synthesized in two steps under high-pressure conditions. Amorphous PtO_2 (99.95%,

dx.doi.org/10.1021/ic501770g | Inorg. Chem. 2014, 53, 11616−11625

Alfa Aesar; and 99.9%, High Purity Chemicals), which exhibits a large volume change under high pressure that often causes blowout using the Kawai-type multianvil setup, was crystallized using the belt-type high-pressure apparatus at the National Institute for Materials Science (NIMS). The commercial powder was sealed in an Au-disk container, which was then placed into a sample cell assembled with a pyrophillite pressure medium, NaCl−20 wt % ZrO_2 cylinder and plugs, thermal insulator, and cylindrical graphite heater. The sample cell was held at 6 GPa and 1073 K for 1 h and quenched to room temperature before the pressure was released.

The product was confirmed to consist of a crystalline $CaCl_2$-type PtO_2 and a small amount of Pt metal using powder X-ray diffraction (XRD) with Cr Kα and Cu Kα radiation (Rigaku, RINT2500 V and PANalytical, X'Pert) and a scanning electron microscope (SEM; JEOL, JSM-6360) equipped with an energy dispersive X-ray spectrometer (EDX; Oxford Instruments, INCA Energy 300). An additional amorphous PtO_2 (85.9 wt % Pt, Furuya Metal) was also tested for preparation of the precursor of the HP-PdF_2-type PtO_2 in the same manner. No significant differences between the final products prepared from the two different kinds of precursors were detected in the XRD, SEM, and EDX characterizations.

Note that a precursor for the HP-PdF_2-type RhO_2 was prepared in the Kawai-type, multianvil, high-pressure apparatus from Rh_2O_3 (99.9%, Alfa Aesar) and $KClO_4$ oxidizer (99.5%, Wako Pure Chemical Industries), which were sealed in a Pt capsule at an approximate volume ratio of 6:1. Tungsten carbide anvils with a truncated edge length of 8 mm were used. The sample cell was heated at 1373 K for 30 min after compressing to 11 GPa, and then, the temperature was quenched before decompression. The recovered product was washed with H_2O to remove KCl, dried thoroughly, and crushed into a powder. The product was confirmed to consist of a mixture of HP-PdF_2- and rutile-type RhO_2 by powder XRD, morphological SEM observation, and EDX compositional analysis. No traces of Rh_2O_3 were detected beyond the background of the characterizations.

The two precursors of HP-PdF_2-type MO_2 (M = Rh, Pt) were heated in the same manner as in the preparation of the three HP-PdF_2-type MO_2 (M = Ru, Os, Ir) in the Kawai-type apparatus. In the second step, the precursors were transformed into HP-PdF_2-type oxides in the Kawai-type apparatus using second-stage anvils with a truncated edge length of 5 mm. The cell containing the precursor was kept at an elevated pressure of 17 GPa and 1073 K for RhO_2 and 1173 K for PtO_2 for 30 min.

Each final product was recovered under ambient conditions, followed by characterization using powder XRD, SEM, and EDX.

2.2. Crystal Structure Characterizations. Synchrotron powder XRD data for the MO_2 compounds (M = Ru, Rh, Os, Ir, Pt) were collected at room temperature using a SPring-8 BL15XU, NIMS beamline, with a Debye−Scherrer camera and imaging plate. The measured incident X-ray wavelength was 0.65298 Å from X-ray absorption near the edge for Nb and XRD from a standard material of the fluorite-type CeO_2.[28] A fine powder of each sample was placed in a Lindenmann glass capillary having a diameter of 0.2 mm for RuO_2, RhO_2, OsO_2, and IrO_2 and a 0.1 mm capillary for PtO_2. The synchrotron XRD data were recorded in a 2θ range of 3−55° at a step interval of 0.003°. The absorption coefficient of each sample was measured using an ion chamber. The estimated μR values ((linear absorption coefficient) × (capillary radius)) from a direct-beam measurement were refined using Rietveld analysis.

The synchrotron XRD patterns were analyzed through a Rietveld refinement method[29] using the software RIETAN-FP.[30] The split pseudo-Voigt function of Toraya[31] was used as the profile function.

A selected sample was studied using transmission electron microscopy (TEM; JEOL, JEM-2010) at the NIMS. The sample was ground into a fine powder, which was mounted on a Cu grid (200 mesh). Carbon was sputtered onto the surfaces prior to imaging. Selected-area electron diffraction (SAED) patterns and high-resolution TEM (HRTEM) images were successfully obtained at room temperature.

2.3. Physical Properties Measurements. The electrical resistivity (ρ) of sintered polycrystalline pellets of each of the final products was measured using a standard four-probe technique with a gauge current of 80 mA for RuO_2, 20 mA for IrO_2, and 1 mA for RhO_2 and OsO_2. Note that the ρ value of PtO_2 was too high to be measured correctly in the instrument, even at room temperature. Silver wires and silver paste were used to fix the electrical contact on the pellet. The measurements were conducted on cooling and warming in a temperature (T) range of 10−300 K. The T dependence of the magnetization (M) of the samples was measured in a commercial magnetometer (MPMS, Quantum Design Inc.) at 5−400 K in a magnetic field of 50 kOe. Isothermal magnetization at 5 and 300 K was recorded with an applied magnetic field between −50 and 50 kOe. The heat capacity at constant pressure (C_p) of the samples was recorded in a commercial thermal-relaxation-type calorimeter (PPMS, Quantum Design Inc.) in a T range of 2−300 K for PtO_2 and 2−30 K for the other compounds.

3. RESULTS AND DISCUSSION

In the XRD patterns of all MO_2 samples, the observed Bragg peaks of each high-pressure phase were indexed on the basis of cubic symmetry: $Pa\bar{3}$ space group. Since the high-pressure phase of RuO_2 was reported to adopt the HP-PdF_2-type structure with the $Pa\bar{3}$ space group,[32] the crystal structure of the other high-pressure phases is HP-PdF_2 type as well. Figure 2a shows the

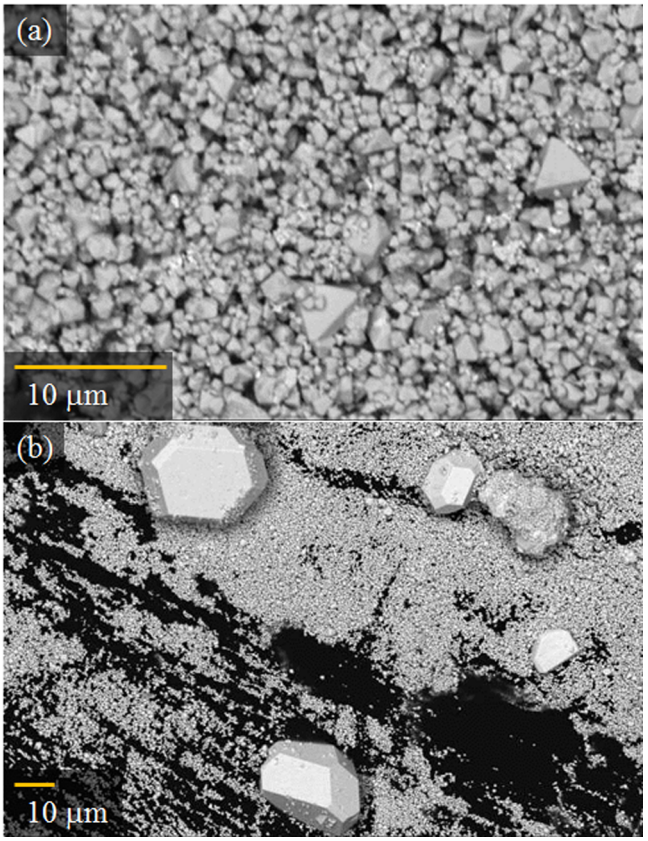

Figure 2. Backscattered electron images of (a) HP-PdF_2-type OsO_2 and (b) PtO_2.

SEM backscattered electron image of the high-pressure-synthesized OsO_2 as a representative sample; octahedral shapes are found to be characteristic and common to all final products except PtO_2, which exhibits a different polyhedral shape, as shown in Figure 2b. The morphology of these crystals is similar to that of pyrite.[33] The SEM-EDX compositional analysis for OsO_2 and PtO_2 indicated that both are stoichiometric; the atomic ratio M:O was 1.00(1):2.00(7). Hence, atom occupancies for all crystallographic sites were fixed in the Rietveld refinements for the five oxides, as will be described below.

dx.doi.org/10.1021/ic501770g | Inorg. Chem. 2014, 53, 11616−11625

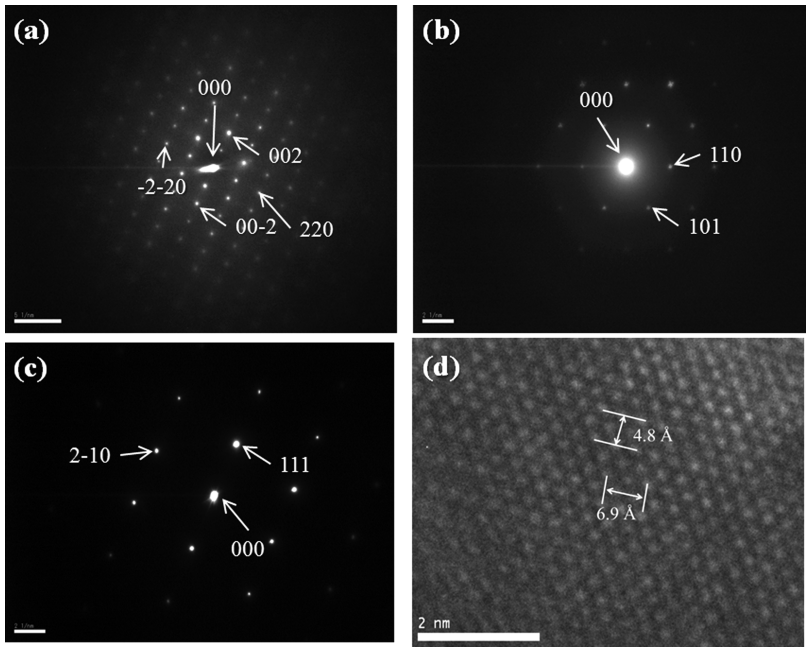

Figure 3. (a–c) SAED patterns of the HP-PdF_2-type PtO_2 taken along the zone axis of (a) [110], (b) [111], and (c) [123]. (d) Corresponding HRTEM image taken along the (110) plane.

Table 1. Structural Parameters and *R* Indices of HP-PdF_2-Type MO_2 (M = Ru, Rh, Os, Ir, Pt)[a]

	RuO_2	RhO_2	OsO_2	IrO_2	PtO_2
			Lattice Constants		
a (Å)	4.85213(1)	4.84563(2)	4.89561(1)	4.89057(2)	4.90683(1)
V (Å^3)	114.2345(5)	113.7760(6)	117.3331(2)	116.9710(9)	118.1418(2)
V_m (cm^3 mol^{-1})	17.19841(8)	17.12938(9)	17.66491(3)	17.61040(13)	17.78667(3)
			Fractional Coordinates and Isotropic Atomic Displacement Parameters		
			M (4a) (0, 0, 0)		
B_{iso} (Å^2)	0.381(1)	0.328(1)	0.297(1)	0.385(1)	0.227(1)
			O (8c) (x, x, x)		
x	0.3495(1)	0.3538(1)	0.3482(3)	0.3458(2)	0.3400(3)
B_{iso} (Å^2)	0.474(9)	0.438(5)	0.658(15)	0.433(14)	0.555(9)
			Global and HP-PdF_2-Type Phase-Dependent Reliability Values and Goodness of Fit Indicators		
R_{wp} (%)	5.668	6.796	3.834	2.395	3.092
R_e (%)	0.514	0.591	0.355	0.269	0.282
R_B (%)	1.696	1.289	1.445	2.330	2.906
R_F (%)	0.907	1.255	0.808	1.322	1.817
			Product of Linear Absorption Coefficient (μ) and Capillary Radius (R)		
μR_{obs}	0.54477	0.45975	1.44754	2.13455	1.52675
μR_{fix}	1.6	1.6	2.5	3.3	1.52675

	rutile RuO_2	rutile RhO_2	rutile OsO_2	rutile IrO_2	Pt_3O_4[d]
			Mass Fraction and Reliability Values for Impurities		
wt %	8.0	3.7	4.2	4.7	8.1
R_B (%)	1.363	0.990	0.978	1.892	4.023
R_F (%)	0.431	0.467	5.9	0.805	2.002
		$Pt_{0.8}Rh_{0.2}O_2$[b]	Os metal[c]		
wt %		1.9	0.9		
R_B (%)		0.447	0.474		
R_F (%)		0.271	8.1		

[a]Space group $Pa\bar{3}$ (No. 205), Z = 4. [b]HP-PdF_2 type. [c]HCP phase. [d]$Pm\bar{3}n$ phase.

Figure 3a–c shows the SAED patterns of the final PtO_2 product as a typical example. In Figure 3a, the $hh0$ and $00l$ diffraction spots, in which both h and l are odd integers, can be clearly observed. Not only the expected Bragg spots of $Pa\bar{3}$ but also extra reflections exist in the pattern. These results seem to be inconsistent with the $Pa\bar{3}$ space group. The spots vanished when the zone axis was slightly tilted from the [110] direction. In addition, any extra Bragg spots disappeared in the SXRD patterns. This confirms that the spots are caused by multiple reflections of the electron beam. Figure 3d exhibits the HRTEM

dx.doi.org/10.1021/ic501770g | Inorg. Chem. 2014, 53, 11616–11625

image of the PtO_2 sample observed from the (110) plane, where white dots correspond to Pt atoms. Throughout the SAED and HRTEM observations, there was no evidence of structural disorder and superlattice formation. Thus, the $Pa\bar{3}$ space group most likely describes the structure of PtO_2.

The fractional coordinates of the HP-PdF_2-type RuO_2[32] and pyrite[34] were used to refine the parameters of the final products of RuO_2, RhO_2, OsO_2, IrO_2, and PtO_2. The refinements readily converged well with reliability values of 7% for R_{wp}, 3% for R_B, and 2% for R_F. The refined structure parameters are summarized in Table 1. The refined patterns and structure images are displayed in Figure 4. The SXRD, SAED, and HRTEM analyses indicated that the $Pa\bar{3}$-type model could reasonably characterize the structure of the final products of all MO_2 compounds.

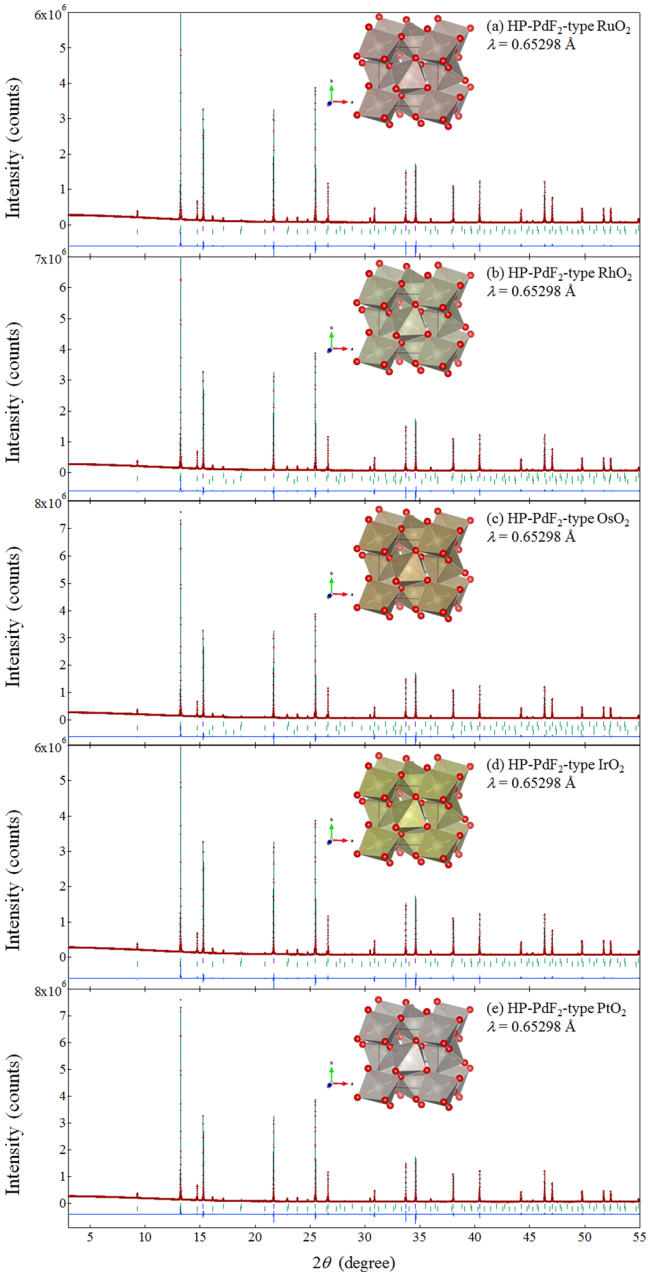

Figure 4. Rietveld refinements of the synchrotron XRD patterns at λ = 0.65298 Å for HP-PdF_2-type MO_2: M = (a) Ru, (b) Rh, (c) Os, (d) Ir, (e) Pt. Polyhedra represent octahedrally coordinated MO_6.

Moreover, the interatomic distances were found to be reasonable, which will be discussed in the next paragraph.

Selected interatomic distances and bond angles are shown in Table 2. All M−O bond lengths are comparable with the sum of the effective ionic radii of $^{VI}M^{4+}$ ($^{VI}Ru^{4+}$, 0.62 Å; $^{VI}Rh^{4+}$, 0.60 Å; $^{VI}Os^{4+}$, 0.63 Å; $^{VI}Ir^{4+}$, 0.625 Å; $^{VI}Pt^{4+}$, 0.625 Å) and O^{2-} (1.40 Å),[35] reflecting the reasonable structure solutions. Incidentally, the interatomic distances of M−O and lattice constants for the high-pressure phases of all MO_2 compounds seem to be characterized by outer-shell (4d and 5d) orbitals, i.e., the distance and lattice constant of RuO_2 are more similar to those of RhO_2 than those of IrO_2 and PtO_2 while the ionic radius of Ru^{4+} is less similar to that of Rh^{4+} than those of Ir^{4+} and Pt^{4+}. The shortest O−O bond is longer than 2.4 Å, indicating the absence of covalent O−O bonding, which would have a much shorter bond length. For example, the covalent O−O bond length is less than 1.5 Å in NaO_2 (1.324 Å[20]), MgO_2 (1.492 Å[21]), ZnO_2 (1.468 Å[22]), and CdO_2 (1.487 Å[25]). The O−M−O bond angles are approximately 82°, indicating that the MO_6 octahedra are slightly distorted from the regular octahedron. The M−O−M bond angles are approximately 120°, indicating that OM_3 forms a regular triangular plane. This structural analysis provides further detailed evidence that the $Pa\bar{3}$-type MO_2 is not pyrite type but HP-PdF_2 type because of the absence of O−O bonding.

Figure 5 shows the T dependence of the direct-current ρ value of each polycrystalline pellet of the HP-PdF_2-type MO_2 (M = Ru, Rh, Os, Ir). The ρ value of PtO_2 was found to be highly insulating beyond the instrumental limit, even at room temperature ($\gg 1 \times 10^4$ Ω cm). All ρ data show metallic-like T dependence over the whole T range studied. Small gaps between the cooling and heating curves might reflect the influence of complicated conduction through grain boundaries. Indeed, the room-temperature ρ values widely vary among the compounds with no reasonable correlation, suggesting that the conduction was complicated to an extent by the polycrystalline nature. A much lower influence of the grain boundaries on conduction is observed for RuO_2 in comparison to the other compounds. The ρ value of RuO_2 is ~1.2 mΩ cm at room temperature, which approaches the common values observed for metallic polycrystalline oxides. In addition, the T dependence of ρ for RuO_2 is well characterized by a Fermi liquid feature, $\rho = \rho_0 + AT^2$, where A is a coefficient, as shown in the inset of each panel of Figure 5. Thus, it can be concluded that the electrical conduction of RuO_2 is metallic in nature. However, the other compounds show relatively poor fitting to the Fermi liquid feature, suggesting that the conduction is complicated by scatterings by grain boundaries. Further studies using a high-quality single crystal are necessary in order to correctly evaluate the true conduction of the high-pressure phases. Table 3 includes roughly estimated A and ρ_0 values of all HP-PdF_2-type MO_2 species in the studies of the polycrystalline compounds.

The magnetic susceptibility (χ) values as a function of T, measured in a magnetic field of 50 kOe, for all HP-PdF_2-type MO_2 are presented in Figures 6a−6e. The Langevin diamagnetic contribution was subtracted from the raw data. The data for the field cooled (FC) process almost follow the zero-field cooled (ZFC) curve for all samples, suggesting the absence of magnetic long-range order over the T range. The data for RuO_2 and IrO_2 show less T-dependent features, suggesting that Pauli paramagnetism is dominant. Thus, the magnetic features are consistent with the metallic behavior observed for the compounds. In contrast, the χ data for RhO_2, OsO_2, and PtO_2 exhibit a degree of T-dependence; thus, the Curie−Weiss (CW)

dx.doi.org/10.1021/ic501770g | Inorg. Chem. 2014, 53, 11616−11625

Table 2. Interatomic Distances and Bond Angles of HP-PdF_2-Type MO_2 (M = Ru, Rh, Os, Ir, Pt)[a]

	RuO_2	RhO_2	OsO_2	IrO_2	PtO_2
			Bond Lengths (Å)		
M−O	1.9855(1)	1.9857(1)	2.0026(1)	1.9993(1)	2.0040(1)
O^i−O^{ii}	2.529(2)	2.454(2)	2.574(5)	2.613(3)	2.720(5)
BVS[b]	3.984	3.565[c]	3.575	4.230	4.280
			Bond Angles (deg)		
M−O−M	119.535(6)	119.261(10)	119.608(15)	119.726(9)	119.921(7)
O^i−M−O^{iii}	82.228(12)	82.685(15)	82.08(3)	81.82(2)	81.17(3)

[a]Symmetry codes: (i) *x*, *y*, *z* (ii) 1−*x*, 1−*y*, 1−*z* (iii) 1/2−*x*, *y*−1/2, *z* [b]BVS = bond valence sum. [c]Calculated from parameters for Rh^{3+} (no available parameters for Rh^{4+}).

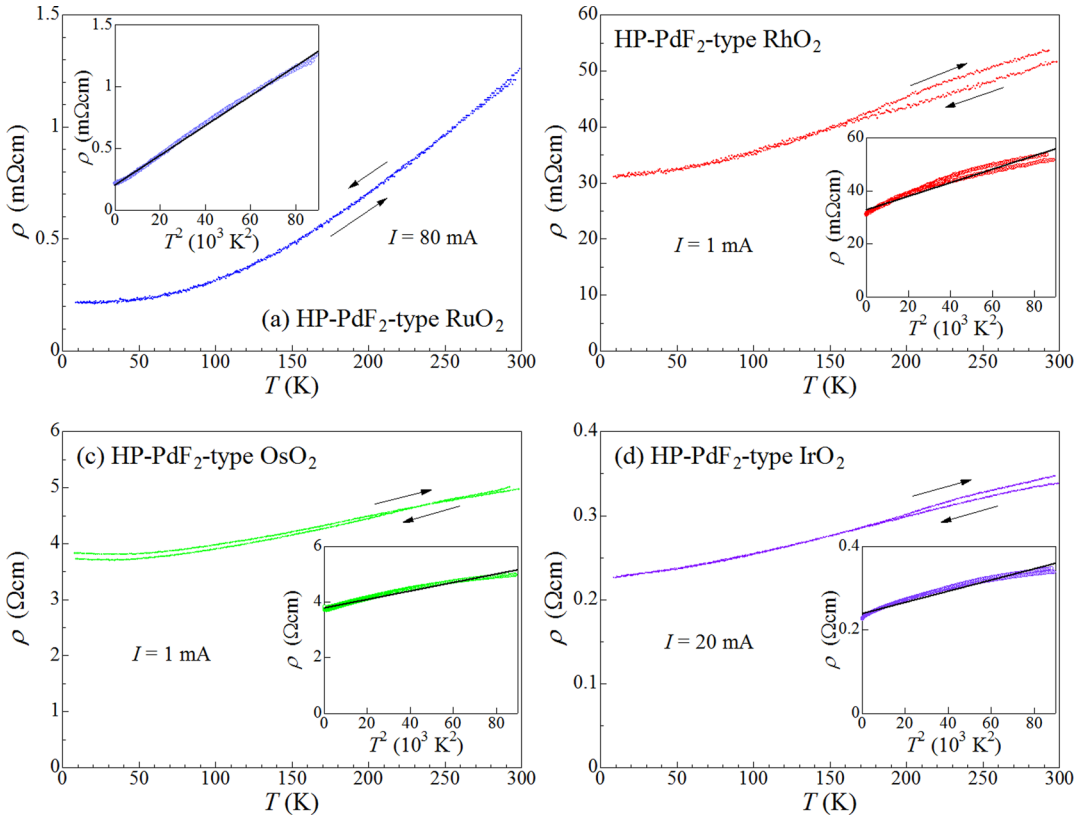

Figure 5. *T* dependence of ρ of the sintered polycrystalline pellet of MO_2: M = Ru (a), Rh (b), Os (c), Ir (d). Insets show alternative plots of the data.

Table 3. Physical Properties of HP-PdF_2-Type MO_2 (M = Ru, Rh, Os, Ir, Pt)

	RuO_2 ($4d^4$)	RhO_2 ($4d^5$)	OsO_2 ($5d^4$)	IrO_2 ($5d^5$)	PtO_2 ($5d^6$)
		Electrical Resistivity			
A ($\mu\Omega$ cm K^{-2})	0.01203	0.2554	15.19	1.337	
ρ_0 (mΩ cm)	0.2054	32.87	3793	239.4	
		Magnetic Constants			
C_{CW} (mJ K mol^{-1} T^{-2})		105	138		45
θ_W (K)		−27.9	−18.4		−4.9
χ_0 (mJ mol^{-1} T^{-2})	2.90	5.83	1.60	5.11	0.85
		Thermal Parameters			
γ (mJ mol^{-1} K^{-2})	5.79	12.22	2.67	11.30	2.39
Θ_D[a] (K)	654	636	479	508	406
		Wilson Ratio and Kadowaki−Woods Rule Value			
R_W (SI unit)	1.83	1.74	2.18	1.65	
A/γ^2 ($\mu\Omega$ cm mol^2 K^2·mJ^{-2})	3.59×10^{-4}	1.71×10^{-3}	2.13	1.05×10^{-2}	

[a]At low-temperature limit.

law was applied in order to analyze this. The analytical CW law is as follows:

dx.doi.org/10.1021/ic501770g | Inorg. Chem. 2014, 53, 11616−11625

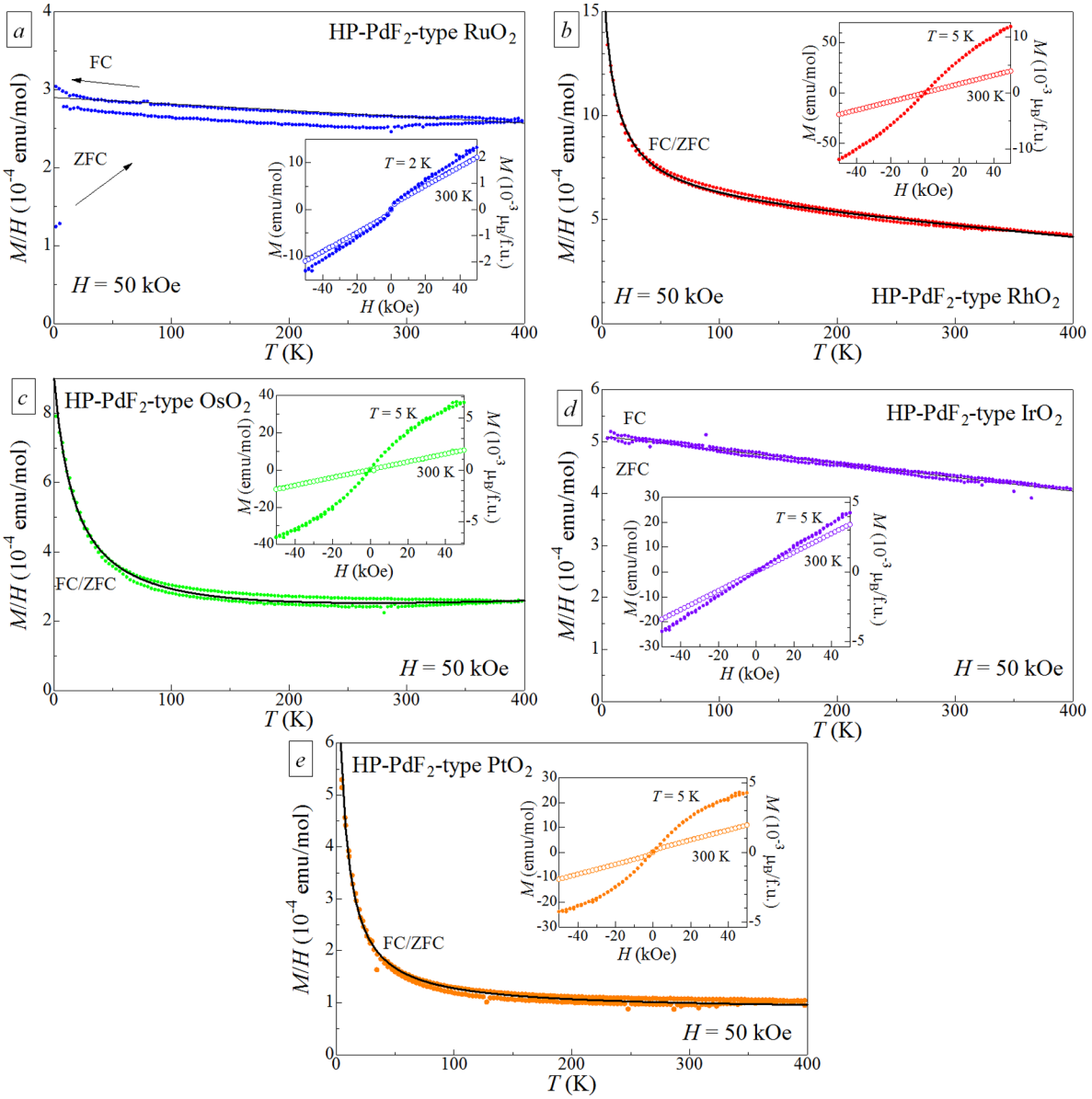

Figure 6. T dependence of M divided by the external magnetic field (M/H) of the sintered polycrystalline pellet of HP-PdF_2-type MO_2: M = Ru (a), Rh (b), Os (c), Ir (d), Pt (e). The applied magnetic field was 50 kOe for all measurements. Insets show isothermal magnetization curves measured at T = 2 (RuO_2), 5 (RhO_2, OsO_2, IrO_2, PtO_2), and 300 K (all).

$$\chi = \frac{C_{CW}}{T - \theta_W} + \chi_0$$

where C_{CW} is the Curie constant, θ_W is the Weiss T, and χ_0 is a T-independent term. This was applied to each data set by the least-squares method, which is shown as a solid curve in each panel of Figure 6. The estimated parameters are summarized in Table 3. In addition, isothermal magnetization has been measured for all samples (insets in Figure 6) and shows no spontaneous magnetic moments at the T values measured. Considering the CW parameters and magnetization data, it is difficult to clearly identify the origin of the T dependence of χ. It is possible that neutron studies may provide significant information about the magnetism. Alternatively, it is likely that magnetic impurities are slightly responsible for the T dependence. The χ_0 value estimated by extrapolation of the Pauli paramagnetic curves to 0 K is used in later discussions. Note that the weak paramagnetic behavior of the HP-PdF_2-type PtO_2 is probably caused by impurity phases including Pt metal and Pt_3O_4.

Figure 7a indicates C_p/T against T^2 at low T for all HP-PdF_2-type MO_2. In the low-T range, far below the Debye temperature, Θ_D, the Debye function can be approximated as

$$\frac{C_v}{T} = \gamma + \left(\frac{12\pi^4 n_{fu} N_A k_B}{5\Theta_D^3}\right) T^2$$

where C_v, n_{fu}, and γ are the heat capacity at constant volume, the number of atoms per formula unit, and the Sommerfeld coefficient, respectively. The analytical formula was applied to the C_p/T vs T^2 curves because C_v is approximately equal to C_p in the low-T range. The values of γ and Θ_D estimated using the least-squares method are given in Table 3. The γ values vary between 2.4 and 12.2 mJ mol^{-1} K^{-2}, which is consistent with the metallic conduction experimentally observed. However, the value of γ for PtO_2 does not account for the electrically insulating

dx.doi.org/10.1021/ic501770g | Inorg. Chem. 2014, 53, 11616−11625

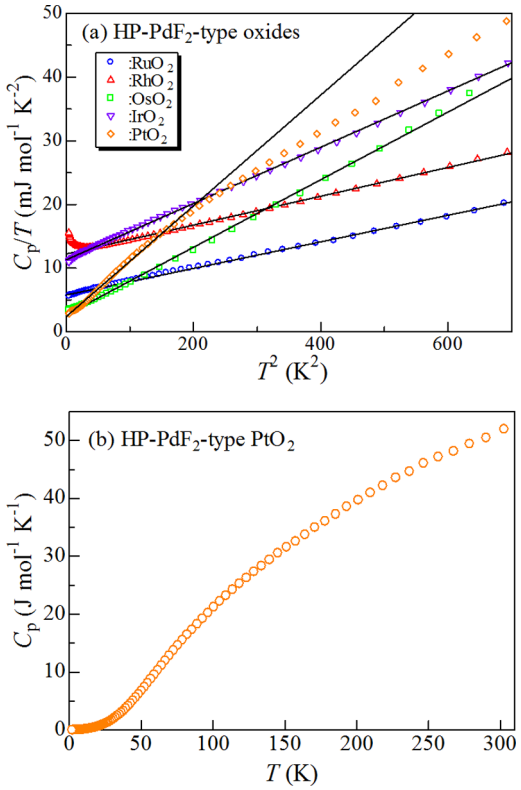

Figure 7. (a) C_p/T against T^2 for HP-PdF_2-type MO_2 (M = Ru, Rh, Os, Ir, Pt). (b) T dependence of the C_p values of the HP-PdF_2-type PtO_2.

features. It is expected to be 0, as PtO_2 has no unpaired electrons ($5d^6$ t_{2g}^6) and is highly electrically insulating. The observed nonzero γ (2.39 mJ mol^{-1} K^{-2}) might be contributed by unidentified factors rather than conduction electrons. The values of Θ_D are in the range 400−660 K, and that for RuO_2 (654 K) is remarkably smaller than the theoretically estimated values of 1436−1707 K.[36] Figure 7b shows the T dependence of C_p for the HP-PdF_2-type PtO_2. The Θ_D value of PtO_2 was alternatively estimated by analyzing the high-T data using only the Debye formula

$$C_{\text{lattice}} = 9n_{\text{fu}}N_A k_B\left(\frac{T}{\Theta_D}\right)^3\int_0^{\Theta_D/T}\frac{x^4e^x}{(e^x-1)^2}\,dx$$

where C_{lattice} and x are the heat capacity of the phonon and a parameter in the integrand, respectively. A relatively high T dependence of Θ_D is obtained as shown in Figure S1 (Supporting Information), suggesting that the Debye model insufficiently describes the C_p of the HP-PdF_2-type PtO_2. The vibrational dispersion relations of the HP-PdF_2-type structure might be fairly complicated. Further experimental studies such as Raman spectroscopy and infrared absorption are needed to correctly evaluate the Θ_D of the HP-PdF_2-type PtO_2. For reference, C_p values for the HP-PdF_2-type PtO_2 are provided in Table S1 (Supporting Information). These data are practically useful for estimating the lattice contribution of the HP-PdF_2-type oxides, as Pt^{4+} is nonmagnetic and, hence, complex magnetic contribution to the lattice is absent.

The Wilson ratio

$$R_W \equiv \frac{4\pi^2}{3}\frac{k_B^2}{g^2\mu_B^2}\frac{\chi_0}{\gamma}$$

where g and μ_B are Landé's gyromagnetic factor and the Bohr magneton, respectively, is often useful for discussing the electronic properties of metallic materials.[37] The estimated R_W values for the HP-PdF_2-type MO_2 (M = Ru, Rh, Os, Ir) are 1.7−2.2 (Table 3) from the experimentally acquired χ_0 and γ values. These are larger than expected for a free electron gas (1.0), suggesting that the high-pressure phases are highly correlated metals.

The Kadowaki−Woods ratio, A/γ^2, is often used to evaluate Fermi-liquid behavior.[38,39] The ratio is generally expected to be between a_0 and $0.04a_0$, where a_0 is a universal constant of 1.0×10^{-5} $\mu\Omega$ cm K^2 mol^2 mJ^{-2}. The experimental ratios for the present high-pressure phases are, however, 1−5 orders of magnitude larger than the expected values (Table 3). This tendency toward overestimation is probably due to the difficulty of evaluating the parameter A using the polycrystalline pellets. Further studies using high-quality single-domain crystals are necessary for an accurate determination of the A/γ^2 values for the compounds.

The electric and magnetic properties of all HP-PdF_2-type MO_2 values are compared with those of the pyrite-type TX_2 (T = late transition metal, X = chalcogen) compounds in Table 4. Overall, remarkable features such as superconductivity and magnetic ordering are absent in HP-PdF_2-type oxides, probably in part because the X_2 dimer, corresponding to the T−X−X−T electronic paths, is not formed. HP-PdF_2-type oxides can be essentially characterized as paramagnetic metals (except for a band insulator of PtO_2). In contrast, a magnetic long-range order in an insulating phase has been established in several pyrite-type 3d transition-metal disulfides at low T, suggesting that their U/W values are much larger than those for HP-PdF_2-type MO_2 oxides. It can be understood that this is caused by the fact that the more broadly extended d shells of the 4d and 5d transition atoms, in comparison with those of the 3d atoms, decrease U. Furthermore, Δ/W', where Δ is the charge transfer energy and W' is the summation of half the bandwidths of the metal and anion, is important for characterizing electronic properties as well as U/W. Generally, Δ decreases sharply upon replacing a divalent cation with a tetravalent cation. Thus, the HP-PdF_2-type MO_2 (M = Ru, Rh, Os, Ir), in which all Ms are tetravalent, is likely to have a stronger tendency toward being metallic in comparison to the pyrite-type TX_2 in this regard. Finally, the comparison suggests that HP-PdF_2-type MO_2 oxides have much smaller U/W and/or Δ/W' values than those of the pyrite-type TX_2.

4. CONCLUSIONS

In summary, we have successfully synthesized polycrystalline compounds of HP-PdF_2-type MO_2 (M = Ru, Rh, Os, Ir, Pt) under high-pressure conditions and characterized the crystal structure and electromagnetic properties by XRD, SEM, EDX, SAED, HRTEM, and measurements of ρ, χ, and C_p. The refined structures clearly indicated that the compounds all crystallized into the HP-PdF_2-type rather than the pyrite-type structure. To the best of our knowledge, the HP-PdF_2-type MO_2 (M = Rh, Os, Pt) compounds have been synthesized for the first time. The HP-PdF_2-type MO_2 (M = Ru, Rh, Os, Ir) exhibited metallic conduction, while PtO_2 did not, likely because the t_{2g} band is filled by 5d electrons. Unfortunately, neither superconductivity nor magnetic order was detected above 2 K in the present compounds. It is possible that U/W and/or Δ/W' are slightly smaller than those of the characteristic chalcogenides. Furthermore, the newly synthesized compounds may be useful to geophysical studies, since they are analogous to the "HP-PdF_2-

dx.doi.org/10.1021/ic501770g | Inorg. Chem. 2014, 53, 11616−11625

Table 4. Comparison of Electronic Properties between HP-PdF_2-Type MO_2 (M = Ru, Rh, Os, Ir, Pt) and Pyrite-Type Transition-Metal Chalcogenides[a]

			transport and magnetic properties[b]		
compound	structure	electronic state			ref
MnS_2	pyrite	Mn^{2+}; d^5 ($t_{2g}^3e_g^2$)	Mott I	AF (T_N = 48.2 K)	40, 41
$MnSe_2$	pyrite	Mn^{2+}; d^5 ($t_{2g}^3e_g^2$)	Mott I	AF (T_N = 47.4 K)	41, 42
$MnTe_2$	pyrite	Mn^{2+}; d^5 ($t_{2g}^3e_g^2$)	Mott I	AF (T_N = 87.2 K)	40, 41
FeS_2	pyrite	Fe^{2+}; d^6 (t_{2g}^6)	band I	van Vleck P + D	11, 13, 43
$FeSe_2$	pyrite	Fe^{2+}; d^6 (t_{2g}^6)	band I	D	11, 13
$FeTe_2$	pyrite	Fe^{2+}; d^6 (t_{2g}^6)	M?	D	13
RuO_2	*HP-PdF_2*	*Ru^{4+}; d^4 (t_{2g}^4)*	M	PP	this work
RuS_2	pyrite	Ru^{2+}; d^6 (t_{2g}^6)	band I	van Vleck P + D	43, 44
$RuSe_2$	pyrite	Ru^{2+}; d^6 (t_{2g}^6)	band I	D	44
$RuTe_2$	pyrite	Ru^{2+}; d^6 (t_{2g}^6)	band I	D	44
OsO_2	*HP-PdF_2*	*Os^{4+}; d^4 (t_{2g}^4)*	(bad) M	PP + CWP	this work
OsS_2	pyrite	Os^{2+}; d^6 (t_{2g}^6)	band I	D	44
$OsSe_2$	pyrite	Os^{2+}; d^6 (t_{2g}^6)	band I	D	44
$OsTe_2$	pyrite	Os^{2+}; d^6 (t_{2g}^6)	band I	D	44
CoS_2	pyrite	Co^{2+}; d^7 ($t_{2g}^6e_g^1$)	H-M	F ($T_C \approx$ 120 K)	45
$CoSe_2$	pyrite	Co^{2+}; d^7 ($t_{2g}^6e_g^1$)	M	exchange-enhanced CWP	13, 46
$CoTe_2$	pyrite	Co^{2+}; d^7 ($t_{2g}^6e_g^1$)	M	PP	13
RhO_2	*HP-PdF_2*	*Rh^{4+}; d^5 (t_{2g}^5)*	M	PP + CWP	this work
RhS_2	pyrite	Rh^{2+}; d^7 ($t_{2g}^6e_g^1$)			47
$RhSe_2$	pyrite	Rh^{2+}; d^7 ($t_{2g}^6e_g^1$)	SC ($T_{SC} \approx$ 6 K)[c]	PP	16, 17
$RhTe_2$	pyrite	Rh^{2+}; d^7 ($t_{2g}^6e_g^1$)	SC (T_{SC} = 1.5 K)		16
IrO_2	*HP-PdF_2*	*Ir^{4+}; d^5 (t_{2g}^5)*	M	PP	this work
IrS_2	pyrite	Ir^{2+}; d^7 ($t_{2g}^6e_g^1$)	M		48
$IrSe_2$	pyrite	Ir^{2+}; d^7 ($t_{2g}^6e_g^1$) Ir^{3+}; d^6 (t_{2g}^6)	SC ($T_{SC} \approx$ 6 K)[c]	CF	18
$IrTe_2$	pyrite	Ir^{2+}; d^7 ($t_{2g}^6e_g^1$) Ir^{3+}; d^6 (t_{2g}^6)	SC ($T_{SC} \approx$ 5 K)[c]		18
NiS_2	pyrite	Ni^{2+}; d^8 ($t_{2g}^6e_g^2$)	Mott I canted AF (T_{N2} = 31 K)	AF ($T_{N1} \approx$ 60 K)	10
$NiSe_2$	pyrite	Ni^{2+}; d^8 ($t_{2g}^6e_g^2$)	M	PP	49
$NiTe_2$	pyrite	Ni^{2+}; d^8 ($t_{2g}^6e_g^2$)	M		13
PtO_2	*HP-PdF_2*	*Pt^{4+}; d^6 (t_{2g}^6)*	band I	D (+CWP: impurity)	this work
CuS_2	pyrite[d]	Cu^{+}; d^{10} ($t_{2g}^6e_g^4$)	SC (T_{SC} = 1.5 K)	CWP?	14, 15
$CuSe_2$	pyrite	Cu^{+}; d^{10} ($t_{2g}^6e_g^4$)	SC (T_{SC} = 2.4 K)	canted AF (T_N = 31 K)	14, 15
$CuTe_2$	pyrite	Cu^{2+}; d^9 ($t_{2g}^6e_g^3$)	SC (T_{SC} = 1.3 K)	canted AF (T_N = 26 K)	13, 14
ZnO_2	pyrite	Zn^{2+}; d^{10} ($t_{2g}^6e_g^4$)			22
ZnS_2	pyrite	Zn^{2+}; d^{10} ($t_{2g}^6e_g^4$)	band I	D	13
$ZnSe_2$	pyrite	Zn^{2+}; d^{10} ($t_{2g}^6e_g^4$)	band I	D	13
CdO_2	pyrite	Cd^{2+}; d^{10} ($t_{2g}^6e_g^4$)			25
CdS_2	pyrite	Cd^{2+}; d^{10} ($t_{2g}^6e_g^4$)	band I	D	13
$CdSe_2$	pyrite	Cd^{2+}; d^{10} ($t_{2g}^6e_g^4$)	band I	D	13

[a]Compounds shown in italics are those studied in this work. [b]Abbreviations: I, insulator; H-M, half-metal; M, metal; SC, superconductor; AF, antiferromagnetism; F, ferromagnetism; PP, Pauli paramagnetism; CWP, Curie–Weiss paramagnetism; D, Larmor diamagnetic; CF, charge fluctuation; T_C, Curie temperature; T_N, Néel temperature; T_{SC}, critical temperature. [c]Defective compounds. [d]Second-order-like phase transition at 160 K.

type" SiO_2, which can exist only above a pressure of ~260 GPa. Attempts to grow high-quality single crystals of HP-PdF_2-type MO_2 for further studies are in progress.

■ ASSOCIATED CONTENT

Supporting Information

List of temperature dependence of heat capacity and Debye temperature as a function of temperature for the HP-PdF_2-type PtO_2. This material is available free of charge via the Internet at http://pubs.acs.org.

■ AUTHOR INFORMATION

Corresponding Author

*E-mail for Y.S.: shirako@numse.nagoya-u.ac.jp.

Present Addresses

○Department of Crystalline Material Science, Nagoya University, Furo-cho, Chikusa-ku, Nagoya, Aichi 464-8603, Japan.

◆Institute of Physics, The Chinese Academy of Sciences, Beijing 100190, People's Republic of China.

¶Condensed Matter Physics, Clarendon Laboratory, University of Oxford, Parks Road, Oxford OX1 3PU, United Kingdom.

△Materials Analysis Station, National Institute for Materials Science, 1-2-1 Sengen, Tsukuba, Ibaraki 305-0047, Japan.

Notes

The authors declare no competing financial interest.

■ ACKNOWLEDGMENTS

The authors thank Dr. F. Izumi (NIMS), Prof. I. Yamada (Osaka Prefecture University, formerly Ehime University), and Dr. Y. Qi and Dr. H. Mizoguchi (Tokyo Institute of Technology) for very useful scientific discussions and comments, as well as the staff of BL15XU, NIMS, and SPring-8 for their assistance with the beamline (Proposal No. 2011A4502). This work was supported in part by the World Premier International Research Center Initiative of the Ministry of Education, Culture, Sports, Science, and Technology (MEXT), Grants-in-Aid for Scientific Research (#22340163 and #25287145 to M.A., #24360275 to Y.I., and #25289233 to K.Y.) from the Japan Society for the Promotion of Science (JSPS), the Funding Program for World-Leading Innovative R&D on Science and Technology (FIRST Program) of the JSPS, and Advanced Low Carbon Technology Research and Development Program (ALCA) of the Japan Science and Technology Agency (JST).

■ REFERENCES

(1) Müller, B. G. *J. Fluorine Chem.* **1982**, *20*, 291−299.
(2) Tressaud, A.; Soubeyroux, J. L.; Touhara, H.; Demazeau, G.; Langlais, F. *Mater. Res. Bull.* **1981**, *16*, 207−214.
(3) Momma, K.; Izumi, F. *J. Appl. Crystallogr.* **2011**, *44*, 1272−1276.
(4) Kuwayama, Y.; Hirose, K.; Sata, N.; Ohishi, Y. *Phys. Chem. Miner.* **2011**, *38*, 591−597.
(5) Kuwayama, Y.; Hirose, K.; Sata, N.; Ohishi, Y. *Science* **2005**, *309*, 923−925.
(6) Tsuchiya, T.; Tsuchiya, J. *Proc. Natl. Acad. Sci. U.S.A.* **2011**, *108*, 1252−1255.
(7) Leger, J. M.; Haines, J. *Eur. J. Solid State Inorg. Chem.* **1997**, *34*, 785−796.
(8) Ono, S.; Kikegawa, T.; Ohishi, Y. *Phys. B* **2005**, *363*, 140−145.
(9) Ogawa, S.; Waki, S.; Teranishi, T. *Int. J. Magn.* **1974**, *5*, 349−360.
(10) Ogawa, S. *J. Phys. Soc. Jpn.* **1976**, *41*, 462−469.
(11) Ogawa, S. *J. Appl. Phys.* **1979**, *50*, 2308−2311.
(12) Krill, G.; Lapierre, M. F.; Robert, C.; Gautier, F.; Czjzek, G.; Fink, J.; Schmidt, H. *J. Phys. C* **1976**, *9*, 761−782.
(13) Bither, T. A.; Bouchard, R. J.; Cloud, W. H.; Donohue, P. C.; Siemons, W. J. *Inorg. Chem.* **1968**, *7*, 2208−2220.
(14) Krill, G.; Panissod, P.; Lapierre, M. F.; Gautier, F.; Robert, C.; Eddine, M. N. *J. Phys. C* **1976**, *9*, 1521−1533.
(15) Ueda, H.; Nohara, M.; Kitazawa, K.; Takagi, H.; Fujimori, A.; Mizokawa, T.; Yagi, T. *Phys. Rev. B* **2002**, *65*, 155104.
(16) Matthias, B. T.; Corenzwit, E.; Miller, C. E. *Phys. Rev.* **1954**, *93*, 1415.
(17) Guo, J.-G.; Qi, Y.; Matsuishi, S.; Hosono, H. *J. Am. Chem. Soc.* **2012**, *134*, 20001−20004.
(18) Qi, Y.; Matsuishi, S.; Guo, J.-G.; Mizoguchi, H.; Hosono, H. *Phys. Rev. Lett.* **2012**, *109*, 217002.
(19) Kwizera, P.; Dresselhaus, M. S.; Adler, D. *Phys. Rev. B* **1980**, *21*, 2328−2335.
(20) Carter, G. F.; Templeton, D. H. *J. Am. Chem. Soc.* **1953**, *75*, 5247−5249.
(21) Vannerberg, N. G. *Ark. Kemi* **1959**, *14*, 99−105.
(22) Vannerberg, N. G. *Ark. Kemi* **1959**, *14*, 119−124.
(23) Ono, S.; Tsuchiya, T.; Hirose, K.; Ohishi, Y. *Phys. Rev. B* **2003**, *68*, 014103.
(24) Haines, J.; Leger, J. M.; Schulte, O. *Science* **1996**, *271*, 629−631.
(25) Hoffman, C. W. W.; Ropp, R. C.; Mooney, R. W. *J. Am. Chem. Soc.* **1959**, *81*, 3830−3834.
(26) Roberts, L. E. J.; Walter, A. J. *Colloq. Int. CNRS* **1966**, *154*, 51−59.
(27) Greaux, S.; Gautron, L.; Andrault, D.; Bolfan-Casanova, N.; Guignot, N.; Haines, J. *Am. Mineral.* **2008**, *93*, 1090−1098.
(28) Tanaka, M.; Katsuya, Y.; Yamamoto, A. *Rev. Sci. Instrum.* **2008**, *79*, 075106.
(29) Rietveld, H. M. *J. Appl. Crystallogr.* **1969**, *2*, 65−71.
(30) Izumi, F.; Momma, K. *Solid State Phenom.* **2007**, *130*, 15−20.
(31) Toraya, H. *J. Appl. Crystallogr.* **1990**, *23*, 485−491.
(32) Haines, J.; Leger, J. M.; Schmidt, M. W.; Petitet, J. P.; Pereira, A. S.; da Jornada, J. A. H.; Hull, S. *J. Phys. Chem. Solids* **1998**, *59*, 239−243.
(33) Wang, Q.; Morse, W. *Mar. Chem.* **1996**, *52*, 99−121.
(34) Paszkowicz, W.; Leiro, J. A. *J. Alloys Compd.* **2005**, *401*, 289−295.
(35) Shannon, R. D. *Acta Crystallogr., Sect. A: Found. Crystallogr.* **1976**, *32*, 751−767.
(36) Mehtougui, N.; Rached, D.; Khenata, R.; Rached, H.; Rabah, M.; Bin-Omran, S. *Mater. Sci. Semicond. Process.* **2012**, *15*, 331−339.
(37) Wilson, K. G. *Rev. Mod. Phys.* **1975**, *47*, 773−840.
(38) Kadowaki, K.; Woods, S. B. *Solid State Commun.* **1986**, *58*, 507−509.
(39) Tsujii, N.; Kontani, H.; Yoshimura, K. *Phys. Rev. Lett.* **2005**, *94*, 057201.
(40) Lin, M. S.; Hacker, H., Jr. *Solid State Commun.* **1968**, *6*, 687−689.
(41) Hastings, J. M.; Elliott, N.; Corliss, L. M. *Phys. Rev.* **1959**, *115*, 13−17.
(42) Itoh, H.; Miyahara, S. *J. Phys. Soc. Jpn.* **1977**, *42*, 470−472.
(43) Müller, W.; Bertschat, H. H.; Biedermann, K.; Kowallik, R.; Lahmer-Naim, E.; Mahnke, H.-E.; Seeger, S.; Zeitz, W.-D.; Fiechter, S.; Tributsch, H. *Phys. Rev. B* **1990**, *41*, 8624−8629.
(44) Hulliger, F. *Nature* **1963**, *200*, 1064−1065.
(45) Wang, L.; Chen, T. Y.; Leighton, C. *Phys. Rev. B* **2004**, *69*, 094412.
(46) Inoue, N.; Yasuoka, H. *Solid State Commun.* **1979**, *30*, 341−344.
(47) Sutarno, R.; Knop, O.; Reid, K. I. G. *Can. J. Chem.* **1967**, *45*, 1391−1400.
(48) Munson, R. A. *Inorg. Chem.* **1968**, *7*, 389−390.
(49) Inoue, N.; Yasuoka, H.; Ogawa, S. *J. Phys. Soc. Jpn.* **1980**, *48*, 850−856.

■ NOTE ADDED AFTER ASAP PUBLICATION

This paper was published on the Web on October 22, 2014. Additional corrections were implemented, including changes to Table 1 and replacing Figure 5. The corrected version was reposted on November 3, 2014.